Heavy-liquid metal heat transfer experiment in a 19-rod bundle with grid spacers

J. Pacio[a,*], M. Daubner[a], F. Fellmoser[a], K. Litfin[a], L. Marocco[a,b], R. Stieglitz[a], S. Taufall[a], Th. Wetzel[a]

[a] *Karlsruhe Institute of Technology (KIT), Hermann-von-Helmholtz Platz 1, 73644 Eggenstein-Leopoldshafen, Germany*
[b] *Politecnico di Milano, Department of Energy, via Lambruschini 4, 20156 Milan, Italy*

Article history:
Received 9 December 2013
Received in revised form 14 February 2014
Accepted 27 February 2014

1. Introduction

For the development of innovative nuclear systems with a strong focus on inherent safety, thermal-hydraulics is one of the key disciplines to be further investigated. The study of heavy liquid metals, such as lead-bismuth eutectic (LBE), is of particular interest for activities related with fast reactors and accelerator driven systems. This undertaking is a challenging task due to the particular physical properties of liquid metals (see Appendix A). With Prandtl numbers (Pr) substantially lower than unity, the physical mechanisms dictating the heat transfer are balanced differently than in fluids with $Pr \sim 1$, such as water or air. In the case of liquid metals, molecular thermal conduction plays a much larger role, even at large Reynolds numbers (Re). Consequently, specific experiments are needed for developing models which accurately represent the thermal-hydraulic behavior of liquid-metal flows.

In order to gain a deeper understanding on the heat transfer and the pressure drop in liquid-metal-cooled rod bundles under typical reactor conditions, an experimental campaign has been launched at the Karlsruhe Liquid Metal Laboratory (KALLA) of the Karlsruhe Institute of Technology (KIT). A test-section

* Corresponding author. Tel.: +49 72160826902.

a	apothem of the hexagonal channel [m, mm]
A	cross sectional flow area (m^2)
c_p	specific heat capacity ($J\,kg^{-1}\,K^{-1}$)
C_v	modified drag coefficient
d	rod diameter (m)
d_h	hydraulic diameter, $d_h = 4A\mathcal{P}^{-1}$ (m)
f	Darcy friction factor
g	gravitational acceleration ($m\,s^{-2}$)
K	pressure-drop coefficient, see Eq. (12)
L	length (m)
LBE	lead-bismuth eutectic
$\dot{m}$	mass flow rate ($kg\,s^{-1}$)
m, n	exponents in Eqs. (10) and (13)
Nu	Nusselt number, $Nu=\alpha d_h \lambda^{-1}$
p	pitch (m)
P	pressure (Pa, bar, mbar)
$\mathcal{P}$	wetted perimeter (m, mm)
Pe	Péclet number, $Pe = Re\,Pr = \rho u_b d_h c_p \lambda^{-1}$
Pr	Prandtl number, $Pr = c_p \mu \lambda^{-1}$
Q	total thermal power (W)
q_w	wall heat flux density ($W\,m^{-2}$)
r	curvature radius (m, mm)
Re	Reynolds number, $Re = \rho u_b d_h \mu^{-1}$
T	temperature (K, °C)
u_b	fluid axial bulk velocity ($m\,s^{-1}$)
$\dot{V}$	volumetric flow rate ($m^3\,s^{-1}$, $m^3\,h^{-1}$)
w	minimum distance to the channel wall (m, mm)
x	axial position in the heated region (m)
X	generic primary variable, see Fig. 7
y	distance to the heated wall (m, mm)
y^+	non-dimensional distance to the heated wall
Y	generic secondary variable, see Fig. 7

Greek letters

α	heat transfer coefficient ($W\,m^{-2}\,K^{-1}$)
ΔP	pressure difference (Pa, bar)
ϵ	solidity, $\epsilon = A_p/A$
Φ	hot-spot factor, see Eq. (24)
λ	thermal conductivity ($W\,m^{-1}\,K^{-1}$)
μ	dynamic viscosity ($kg\,m^{-1}\,s^{-1}$)
ρ	Density ($kg\,m^{-3}$
σ_X	standard deviation of X (same as X)
Θ	non-dimensional temperature, see Eq. (23)
Ω_1, Ω_2	temperature-offset coefficients, see Eq. (1) (–, K)

Subscripts

b	refers to the bulk conditions
bdl	refers to the complete rod bundle
corr	corrected value
CT	refers to Cheng and Todreas (1986)
dis	refers to discharge
dyn	refers to dynamic
fric	refers to friction
g	refers to gravity
heat	refers to the heated region
in	refers to the inlet conditions
max	maximum value
min	minimum value
out	refers to the outlet conditions
p	refers to the projected area
raw	raw value
ref	reference value
sch	refers to the internal subchannels
sp	refers to the spacer
st	refers to static
tc	refers to the thermocouple
tot	total value
w	refers to the heated rod wall

consisting of an electrically heated 19-pin rod bundle with three grid spacers was mounted in the test port of the existing THEADES LBE loop. Extensive temperature and pressure drop data are recorded by the installed instrumentation, providing reliable data for understanding this type of geometry and fluid to the scientific understanding of this type of flows, as well as validating predicting numerical models.

The structure of this article is as follows. In Section 2 the setup of these experiments is described in detail. Pressure drop and heat transfer analyses are presented separately in Sections 3 and 4, respectively. A discussion on the outcome of these experiments is given in Section 5, and general conclusions, in Section 6.

2. Experimental setup and procedure

The main characteristics of the test facility are presented in Section 2.1 and those specific of the test section, in Section 2.2. Detailed information about the instrumentation is given in Section 2.3. Section 2.4 describes the data acquisition and reduction scheme, while Section 2.5 covers the test matrix of this experimental campaign.

2.1. The LBE test loop

This experiment has been installed in a test port of the existing THEADES loop at KIT-KALLA, sketched in Fig. 1. The main piping is made of 316 Ti stainless steel in a standard DN-100 size (inner

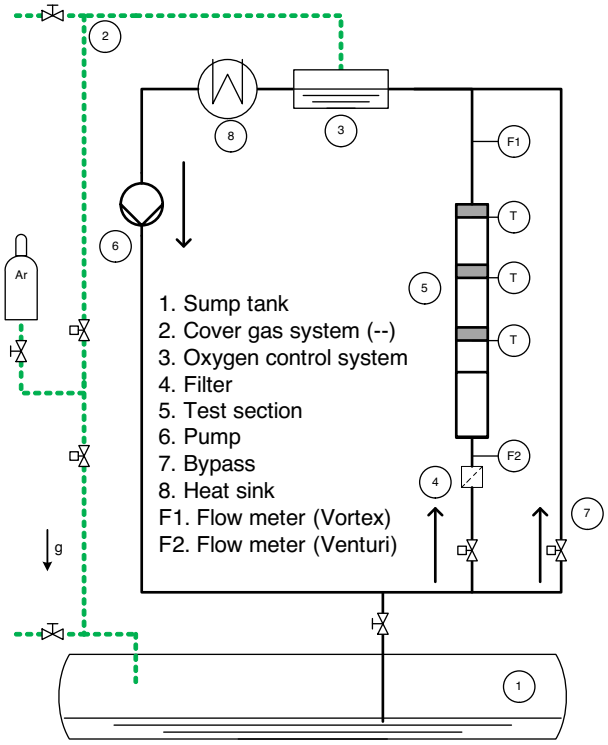

Fig. 1. Schematic representation of the THEADES LBE loop as set-up for this experimental campaign.

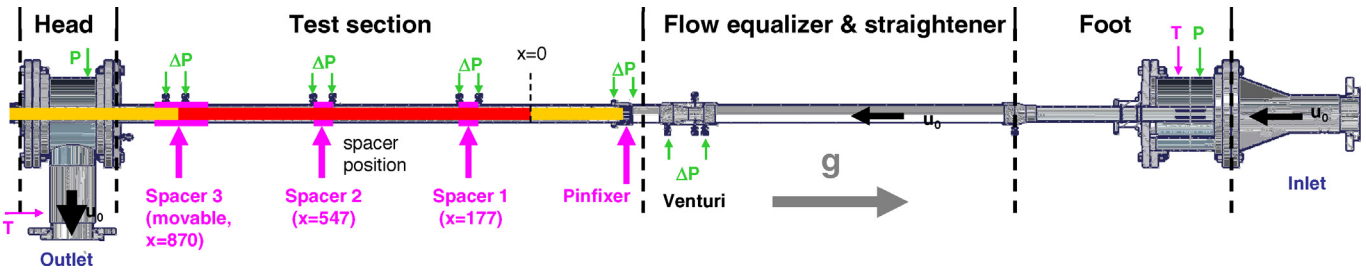

Fig. 2. Side view of the test section. The flow is vertical in the upward direction. All axial positions are expressed in mm, referred to the onset of the heated zone ($x = 0$).

diameter 105.3 mm). Mineral wool (143 mm thick) provides thermal insulation.

A sump tank (position 1) holds the complete LBE inventory (42 tons). After pre-heating the circuit with auxiliary heaters up to the stand-by temperature (200 °C), it is filled with liquid by pressurizing the sump tank with the argon cover gas system (position 2). The inverse action allows to drain the liquid back into the tank. An oxygen control system (position 3) is used for maintaining a constant concentration of diluted oxygen, see Lefhalm et al. (2001), preventing both the formation of lead oxides and an excessive corrosion rate. Under these conditions, steady-state operation up to 450 °C is possible.

In the case of oxygen excess, solid lead-oxide particles might be formed. For that reason, a filter (position 4) is placed at the inlet of the test section (position 5, described in detail in Section 2.2) in order to prevent solid particles from entering the heated zone.

A centrifugal pump (position 6) allows for a maximum volumetric flow rate of 42 $m^3\ h^{-1}$ and a pressure head of 5.9 bar. In order to reduce the circulation time and thus increase the dynamics of the circuit, improving its thermal controllability, a bypass line (position 7) is used. Thus, the flow rate in the test section can be controlled independently from the main flow provided by the pump.

The heat sink corresponds to an air cooler (position 8) with a maximum capacity of 500 kW. In this experimental campaign, heating rates (Q) up to 430 kW were applied to the test section.

Two volumetric flow meters are installed in this loop. A Vortex flow meter (model YOKOGAWA DY050) was placed at the outlet of the test section (position F1). This sensor has an accuracy of 0.75% in its measuring range, between 2.09 and 73.8 $m^3\ h^{-1}$. As experiments at lower flow rates were planned (see Section 2.5), a secondary flow meter of the Venturi type was placed at the inlet of the test section (position F2). This sensor relies on a pressure difference measurement, and this information is translated into flow rate following an in situ calibration.

2.2. The test section: 19-rod bare hexagonal bundle with grid spacers

The test section, installed in the vertical direction with upward flow at the position 5 in Fig. 1, consists of a bundle of 19 electrically heated rods with three grid spacers. This array is embedded in a hexagonal channel with rounded corners. A side view of this construction is shown in Fig. 2.

In the flow direction, the test section foot is placed directly after the filter (position 4 in Fig. 1). As described in Section 2.1, a Venturi nozzle was installed upstream of the test section for complementing the Vortex-type flow meter at lower velocities. A flow equalizer and a straightener section are located upstream of it, in order to obtain a more homogeneous flow distribution over the section and thus a more accurate reading from this sensor.

Downstream of the Venturi nozzle, a pin-fixer is placed and the hexagonal flow channel starts. As this transition and the pin-fixer itself are expected to introduce some perturbations to the velocity profile, they are placed 400 mm upstream of the beginning of the heated zone.

In this hexagonal channel, the 19 rods are placed in a regular array of equilateral triangles. The main parameters of this array are given in Table 1. It should be noted that for this geometry it is possible to define two different hydraulic diameters, $d_h = 4A/\mathcal{P}$, where A is the flow area and $\mathcal{P}$, the wet perimeter.

Firstly, considering the flow area and wet perimeter of the complete bundle array (including the non-heated wall of the hexagonal channel) leads to $d_{h,bdl} = 7.70$ mm. This value is selected for the pressure drop analysis in Section 3. Secondly, considering these parameters for the inner sub-channels leads to $d_{h,sch} = 9.52$ mm. This value is selected for the heat transfer analysis in Section 4 in order to guarantee that these results are comparable with that of other authors.

In the heated region, the rods are kept in position by three grid spacers which, at the same time, provide support for a detailed temperature measurement, see Section 2.3.1. These spacers, shown in Fig. 3 were fabricated by selective laser melting using a rapid-prototyping technique. On the one hand, this construction allows the setup of detailed structures, such as fine channels for supporting the thermocouples at selected locations, see Section 2.3.1. On the other hand, it also results in a relatively large roughness, which was found to be approximately 30 μm.

In a honeycomb structure, three dimples surround each rod and fix its position. The axial positions of the three grid spacers (centerlines) are indicated in Fig. 2. The first two are fixed at $x_{sp,1} = 177$ mm and $x_{sp,2} = 547$ mm, while the third one can be moved around its reference position at $x_{sp,3,ref} = 870$ mm, see Section 5.1.

Table 1
Main dimensions of the 19-rod bundle test section. Inner sub-channels are those numbered 1–24 in Fig. 4.

Dimension	Symbol	Value
Heated rods		
Rod outer diameter	d	8.2 mm
Rod total length	L_{tot}	1272 mm
Rod heated length	L_{heat}	870 mm
Triangular array of 19 rods		
Distance between rod centers (pitch)	p	11.48 mm
Pitch-to-diameter ratio	p/d	1.4
Minimum distance to the channel wall	w	1.716 mm
Hexagonal flow channel		
Apothem	a	25.7 mm
Curvature at the corners	r	3 mm
Flow area	A_{bdl}	1281.71 mm^2
Wet perimeter	$\mathcal{P}_{bdl}$	665.8 mm
Hydraulic diameter	$d_{h,bdl}$	7.70 mm
Inner sub-channel		
Flow area	A_{sch}	30.66 mm^2
Wet perimeter	$\mathcal{P}_{sch}$	12.88 mm
Hydraulic diameter	$d_{h,sch}$	9.52 mm
Grid spacers		
Length	L_{sp}	25 mm
Solidity	ϵ	0.29

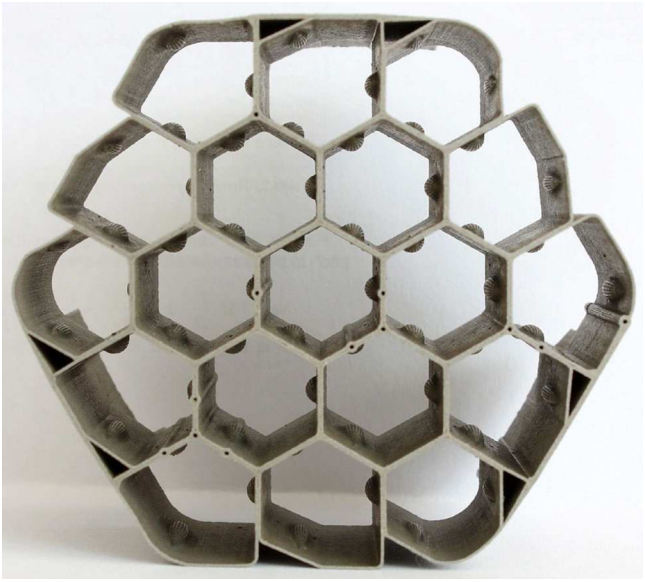

Fig. 3. Bottom-view of the grid spacers (L_{sp} = 25 mm). Throughout the holes at the spacer wall, 38 (13 at the first two spacers and 12 at the third one) thermocouples with d_{tc} = 0.25 mm are inserted at the selected locations indicated in Fig. 4

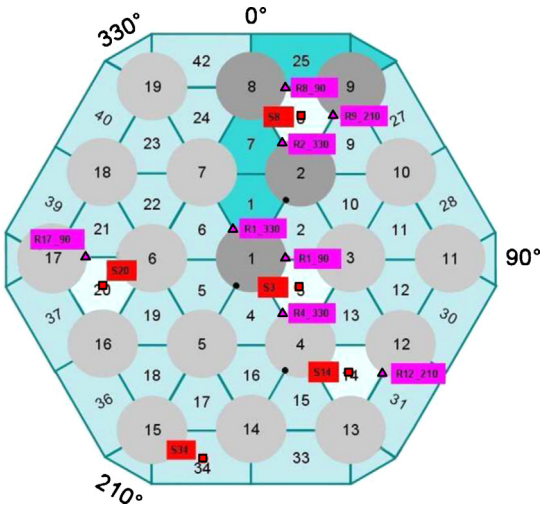

Fig. 4. Schematic representation of the 41 thermocouple positions at the measuring planes in the spacers. *Notes*: magenta triangles: T_w *from outside* (24). Red squares: sub-channel center temperature (14, channel 34 not present at the third level). Black circles: T_w *from inside* (3, only at the third axial position). (For interpretation of the references to color in this figure legend, the reader is referred to the web version of the article.)

At the top, beyond the heated region, connections are provided for both the electrical power and the signal cables of the instrumentation. Each rod has a copper core and a nickel ring where the thermal power is generated, as indicated in Fig. 6. Two layers of boron nitride (BN) provide both electric insulation and radial thermal conduction toward the outer stainless-steel cladding.

2.3. Instrumentation

While the THEADES loop is equipped with extensive instrumentation that allows its control during operation, the present section describes only those measurements performed in the test section itself. For measuring the volumetric flow rate, two sensors were used, as described in Section 2.1. The following paragraphs describe the measurement of temperature and pressure drop at different locations, as well as the thermal power.

2.3.1. Temperature (T)

A total of 46 thermocouples (type K with a steel jacket) was used. All of them were calibrated simultaneously, using the following procedure, with a resulting precision of ±0.1 K. A set of isothermal tests (with $\dot{m} = 0$) at different temperature levels was performed in order to identify the offset of each thermocouple. It is observed that it has a linear dependence on the temperature and, accordingly, two coefficients Ω_1 and Ω_2 are defined. Based on these coefficients, a corrected temperature value (T_{corr}) is derived from the raw value (T_{raw}) as in Eq. (1).

$$T_{corr} = T_{raw} + \Omega_1 + \Omega_2(T_{raw} - T_{ref}) \tag{1}$$

Two thermocouples (d_{tc} = 1 mm in diameter) were placed at the inlet and three at the outlet, for indicating T_{in} and T_{out}, respectively. The remaining 41 were used at the measuring planes of the spacers. These can be divided into three groups, as represented schematically in Fig. 4.

First, represented with magenta triangles, 24 thermocouples (8 in each spacer) with a diameter of d_{tc} = 0.25 mm, are dedicated to measure the wall temperature at selected locations *from outside*. These are supported at the spacer walls and placed 2.5 mm upstream of its lower edge. This means that the three measurement levels for this temperature are x_1 = 162 mm, x_2 = 532 mm and $x_{3,ref}$ = 855 mm.

These thermocouples are mounted on the spacer walls and bent toward the rod wall and are in direct contact with it, under elastic tension, see Fig. 5.

This setup provides an accurate measurement of the wall temperature T_w, although a small correction is needed, considering that the sensing tip is located at its center and thus it remains at a radial distance $y = d_{tc}/2$ from the wall. Given the small distance from the wall and the low Prandtl number of LBE, it can be estimated that these thermocouples are located inside the thermal boundary layer ($y^+\mathrm{Pr} < 1$) (Kirillov and Ushakov, 2001b). Within this layer, a purely molecular conduction analysis applies and the correction is given by Eq. (2).

$$T_{w,corr} = T_{w,raw} + q_w y \lambda_b^{-1} \tag{2}$$

Considering the large temperature gradients (proportional to the wall heat flux density q_w) in this experiment, the correction defined in Eq. (2) is essential for avoiding a systematic error in the evaluation of T_w.

Second, the fluid temperature is measured with 14 thermocouples (d_{tc} = 0.25 mm) placed at the center of the sub-channels indicated as red squares in Fig. 4. Five sub-channels (including a central channel, three symmetrical ones in the first ring and one in the edge) are considered for the first two spacers. Space limitations only allowed for four measurements at the third spacer, thus

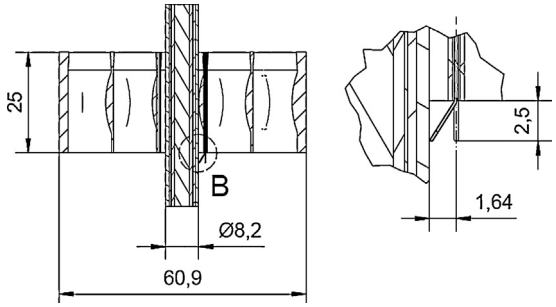

Fig. 5. Geometrical representation of the thermocouples placed at the wall *from outside*. All dimensions are in mm.

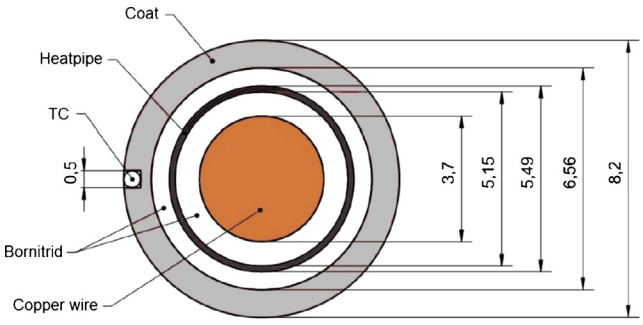

Fig. 6. Schematic representation of the heated rod and the thermocouples inside the cladding. All dimensions are in mm.

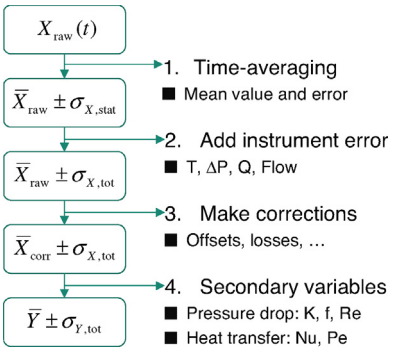

Fig. 7. Four-step data processing strategy.

lacking the measurement at the edge sub-channel, numbered 34 in Fig. 4. These thermocouples were placed at the same level as the measurements for the wall temperature *from outside* (2.5 mm upstream of the spacers). It should be noticed that these measurements indicate the local fluid temperature at the selected locations and not the bulk temperature T_b.

Third, an alternative measuring technique for the rod wall temperature was applied at the third spacer. Three thermocouples with a diameter of $d_{tc} = 0.5$ mm (black circles in Fig. 4) were installed to measure the wall temperature *from inside* the cladding of the heating rod, as sketched in Fig. 6. They are fixed slightly below the third spacer, at $x = 835$ mm.

This alternative technique also requires a correction in order to avoid a systematic error, as a steep temperature gradient (proportional to q_w) exists in the cladding. Considering, as in Fig. 5, that the thermocouple measures the temperature at the junction (located at the center), the correction is given by Eq. (3), where d_{tc} is the thermocouple diameter (0.5 mm) and λ_{tc}, its thermal conductivity.

$$T_{w,corr} = T_{w,raw} - \frac{q_w}{\lambda_{tc}} \frac{d}{2} \ln\left(\frac{d}{d - d_{tc}}\right) \tag{3}$$

It should be noted that, being λ_b and λ_{tc} of similar magnitude, the correction given by (3) is roughly twice as large as the one from Eq. (2). This is a consequence of the larger thermocouple diameter d_{tc}. In that context, extreme caution is required, in particular for high heat fluxes q_w. For liquid metals, the temperature drop through the rod cladding can be comparable with $T_w - T_b$ (Möller and Tschöke, 1972). Thus, a careful evaluation of Eq. (3) is essential to obtain an accurate value of the outer wall temperature.

2.3.2. Pressure drop (ΔP)

Six differential pressure sensors are used in this experimental campaign, representing the ΔP at the pin-fixer, the Venturi nozzle, the three spacers and the complete test section, as indicated in Fig. 2. At the three spacers, the measuring positions of these sensors are located at +50 and −50 mm from their centerline.

In all cases, lines filled with LBE at 200 °C were used for connecting the measuring points to the sensors, placed at a single horizontal level. These sensors are Rosemount 3051 DP transmitters, with a total accuracy of 0.15% of the span, which can be adjusted. Consequently, prior to the experiments, they were tuned according to the expected individual values of ΔP. They were set to 2500 mbar for the complete test section, and 720 mbar for all other measurements.

For the calibration of the ΔP measurements, reference isothermal tests (with $\dot{m} = 0$) were performed and the signals were set to zero. This means that the hydrostatic pressure difference, was inherently accounted for. Nevertheless, in the heated tests, a small correction given by Eq. (4) is required for considering the different hydrostatic pressures given by the changes in density.

$$\Delta P_{corr} = \Delta P_{raw} + [\rho(T_{ref}) - \rho(T_m)]g\Delta x \tag{4}$$

Due to the large density of LBE, this term can be relatively large (a few mbar) and could obscure the other contributions to ΔP, such as distributed friction and lumped drag, especially at low velocities. Thus, the correction in Eq. (4) is essential for the pressure drop analysis presented in Section 3.

2.3.3. Thermal power (Q)

A direct-current power supply is used for heating the rods. Therefore, measuring independently the voltage and current, the electrical power applied to the test section is obtained. In the experiments, it was noticed that this value exceeds the results of a thermal-energy balance, presumably due to unaccounted power losses (both thermal and electrical) outside the test section. Previous authors, e.g. (Johnson et al., 1953), have observed a systematic difference beyond 5% between the electrical and thermal powers. For that reason, the energy balance in Eq. (5) is selected as an accurate representation of the total thermal power applied to the rod bundle.

$$Q = Q_l + \dot{m} \int_{T_{in}}^{T_{out}} c_p(T) dT \tag{5}$$

The thermal losses Q_l are correlated to the temperature level, based on a set of calibration isothermal tests. Based on the value of Q given by Eq. (5), the wall heat flux density q_w is defined by Eq. (6). It can be assumed to be uniformly distributed between the rods and both axially and circumferentially for each rod.

$$q_w = \frac{Q}{19\pi d L_h} \tag{6}$$

2.4. Data acquisition and reduction scheme

After reaching stationary conditions in the LBE loop, data samples were obtained during 3 min for each run, at a sampling rate of 2000 Hz for the temperatures (using a National Instruments PCI-6031E) and 1 Hz for all other variables. In this work, these data are reduced following the four-step strategy shown in Fig. 7.

Each transient raw variable $X_{raw}(t)$ is averaged, yielding a mean value $\overline{X}_{raw}$ and a statistical standard deviation $\sigma_{X,stat}$. An additional uncertainty is given by the accuracy of the instrument $\sigma_{X,instr}$ and, as both are independent, the total standard deviation $\sigma_{X,tot}$ is given by Eq. (7).

$$\sigma^2_{X,tot} = \sigma^2_{X,stat} + \sigma^2_{X,instr} \tag{7}$$

The measured values of the primary variables are then corrected as described in Section 2.3. Based on this information, secondary

Table 2
Envisaged test matrix, in terms of volumetric flow rate ($\dot{V}$, $m^3\,h^{-1}$) and thermal power (Q, kW). *Notes*: – = no experiments. × = T_{in} = 200 °C. ○ = T_{in} = 300 °C.

$\dot{V}$, $m^3\,h^{-1}$	Thermal power Q, kW							
	50	100	150	200	250	300	350	426
1.00	×	×	–	–	–	–	–	–
2.00	×○	×○	×	×	–	–	–	–
4.00	×○	×○	×○	×○	×	×	×	–
5.00	×○	×○	×○	×○	×○	×	×	×
6.00	×○	×○	×○	×○	×○	×○	×	×
8.00	×○	×○	×○	×○	×○	×○	×○	×
9.23	×○	×○	×○	×○	×○	×○	×○	×○
10.00	×○	×○	×○	×○	×○	×○	×○	×○

variables Y are calculated for the pressure drop and heat transfer analyses presented in Sections 3 and 4, respectively.

2.5. Test matrix

The list of planned experiments is summarized in Table 2, in terms of the main operating parameters (Q, $\dot{V}$ and T_{in}). At low flow rates and large thermal powers, the main limitation is given by the outlet temperature which would, in some cases, exceed the upper temperature limit of the THEADES loop (450 °C). Thus, such cases are not studied.

Given the flow area of the hexagonal channel A_{bdl} listed in Table 1, a volumetric flow rate of 9.23 $m^3\,h^{-1}$ corresponds to an axial bulk velocity of $u_b = 2\,m\,s^{-1}$. Throughout the experimental campaign, all cases listed in Table 2 were investigated. Furthermore, additional tests were performed, for calibration purposes.

3. Pressure drop analysis

Some preliminary considerations for this analysis are presented in Section 3.1, and the experimental results are studied in Section 3.2.

3.1. Evaluation method and previous investigations

The static pressure drop is derived from an energy balance. For the present fuel rod bundle with spacer grids, it is composed of several terms, as in Eq. (8).

$$\Delta P_{st} = \Delta P_{dyn} + \Delta P_g + \Delta P_{fric} + \Delta P_{sp} + \Delta P_{pin} + \Delta P_{dis} \tag{8}$$

The first two terms on the right hand side account for the change in kinetic and potential energy of the fluid, respectively. According to Fig. 2, the other terms represent the irreversible losses due to friction over the bare rods, the local losses at the spacer grid locations, the losses due to the pinfixer and the discharge loss in the vessel. As described in Section 2.3.2, the gravitational contribution is inherently accounted for and thus $\Delta P_g = 0$ in Eq. (8).

In this work, the contributions of both the distributed friction ΔP_{fric} and the lumped pressure drop at the spacers ΔP_{sp} are studied. For a bare rod bundle the friction pressure loss along an axial distance Δx can be calculated from the Darcy–Weisbach formula as in Eq. (9), where ρ and u_b are evaluated at the mean temperature along the flowpath.

$$\Delta P_{fric} = \frac{1}{2} f \frac{\rho u_b^2}{d_{h,bdl}} \Delta x \tag{9}$$

Over the years, several correlations, both theoretical and empirical, have been proposed for evaluating the coefficient f. A milestone is the work of Rehme (1972) which has been subsequently extended and completed by Cheng and Todreas (1986) (CT), who derived friction-factor correlations applicable to both bare and wire-wrapped hexagonal and square rod bundles. They follow the general Eq. (10), where the coefficient n assumes different values for laminar and turbulent flow and C is a coefficient dependent on the bundle geometry, i.e. p/d ratio and rod arrangement. The Reynolds number is calculated as in Eq. (11), where the physical properties are evaluated at the arithmetic mean bulk temperature between the inlet and the outlet of test section.

$$f_{CT} = \frac{C}{\mathrm{Re}^n} \tag{10}$$

$$\mathrm{Re} = \frac{\dot{m}}{A_{bdl}} \frac{d_{h,bdl}}{\mu} \tag{11}$$

with μ at $(T_{in} + T_{out})/2$

At the three grid spacers, the lumped pressure drop is evaluated in terms of the coefficient K_{sp}, given by Eq. (12). It should be noted that, as mentioned in Section 2.3, the pressure drop measurements are taken over an axial distance larger than the spacers themselves. Therefore, in order to evaluate the pressure loss coefficient of the spacer alone, the contribution of the frictional losses (based on f_{CT}) over $\Delta x = 75$ mm is subtracted.

$$K_{sp} = \frac{\Delta P_{sp}}{0.5 \rho u_b^2} - f_{CT} \frac{\Delta x_{sp}}{d_{h,bdl}} \tag{12}$$

Several models for the spacer pressure drop have been proposed over the years. Most of them assume, as proposed by Rehme and Trippe (1980) that the main dominating factor is the spacer solidity $\epsilon = A_p/A_{bdl}$, that is the ratio between the projected cross section of the spacer grid to the bundle cross section. In the present experimental setup, as shown in Fig. 3, the rods are positioned by point contacts embossed in the honeycombs to compensate lateral and axial expansion of the rods. The thickness of the inner walls of the grid spacer remains constant for the first 20.5 mm and then increases linearly in the last 4.5 mm up to the downstream surface, in order to accommodate the temperature sensors. This leads to an average solidity for the honeycomb structure without embossed point contacts of $\epsilon = 0.29$.

Based on this assumption, these correlations rely on a constant exponent m and a modified drag coefficient C_v which depends on the Reynolds number and the spacer geometry, as in Eq. (13).

$$K_{sp} = (\mathrm{Re}, \mathrm{geometry}) \epsilon^m C_v \tag{13}$$

In their recent work, Chenu et al. (2011) tested several correlations based on Eq. (13) against experimental data from a 12-pin bundle with sharp-edge grid spacers, described in Eifler and Nijsing (1980). They found those from Voj et al. (1973) and Epiney et al. (2010), especially designed for sharp edges, to give the best performance. The latter, given by Eq. (14) is derived on the basis of a correlation for rounded edge grid spacers proposed by Cigarini and Dalle Donne (1988), but it accounts for a lower exponent $m = 0.2$ for sharp edges.

$$C_v = 1.104 + \frac{791.8}{\mathrm{Re}^{0.748}} + \frac{3.348 \times 10^9}{\mathrm{Re}^{5.652}} \tag{14}$$

with Re at T_b and $m = 0.2$.

As a possible explanation, they argued that the larger turbulence induced by the sharpness of the edges overcomes the effect of the increased flow blockage.

3.2. Experimental results

Fig. 8 shows the experimentally measured pressure drop coefficient at the spacers, compared with Eq. (14). There is satisfactory agreement for $\mathrm{Re} > 2.5 \times 10^4$, while the large uncertainties at lower Re do not allow to draw conclusions. It should also be noted that the experimental data tend asymptotically toward a constant value of

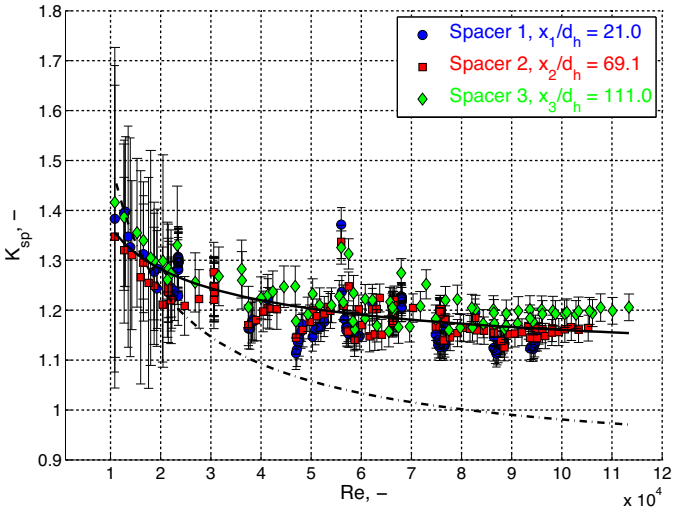

Fig. 8. Spacers pressure loss coefficient. The dot-dashed line refers to Eq. (14) of Epiney et al. (2010) and the solid line to Eq. (15).

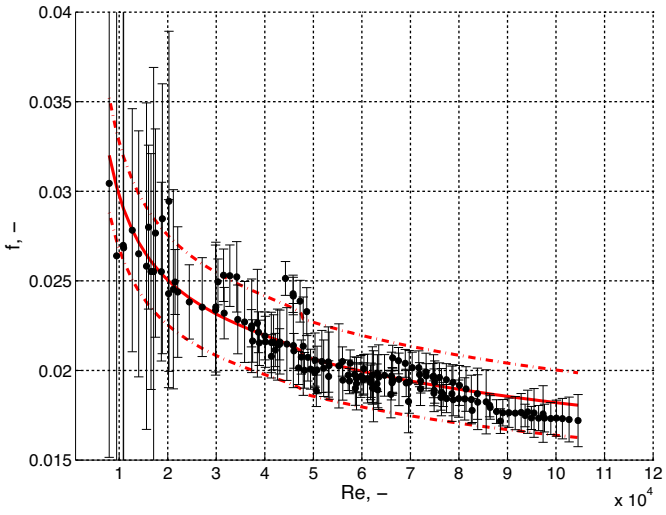

Fig. 9. Experimental rod bundle friction factor *f*. The solid line refers to the correlation of Cheng and Todreas (1986) and the dash-dot lines the deviation of ±10% from it.

K_{sp} at high Re, while the correlation lies below them with a negative slope. The reason could lie in the different manufacturing process of the spacers used in our experimental campaign. Indeed, a selective laser melting process has been used instead of the more common bending and welding of steel plates. The first method results in a much higher roughness compared to the latter, which could explain the decreased dependency from the Reynolds number at high Re values as for fluid flowing in rough ducts.

In their analysis, Epiney et al. (2010) have stated the necessity to tune C_v for new spacer designs. Accordingly we propose Eq. (15) for C_v (considering $m = 0.2$) as a best-fitting of our experimental dataset. It should be noticed that the coefficients in Eq. (15) are remarkably different from those in Eq. (14). In particular, for an infinitely large Re, an 8% higher drag coefficient is predicted by Eq. (15).

$$C_v(\mathrm{Re}) = 1.315 + \frac{9.455}{\mathrm{Re}^{0.407}} + \frac{10.561}{\mathrm{Re}^{0.43}} \tag{15}$$

Based on the experimental information, ΔP_{fric} is evaluated by subtracting all other terms in the right-hand side of Eq. (8) from the total static pressure drop along the test section. In particular, the only contribution that could not be directly measured and thus must be estimated is the discharge loss at the outlet of the test section. This estimation is based on a pressure loss coefficient K_{dis}, as in Eq. (16), where ρ and u are evaluated at the discharge bulk temperature T_{out}.

$$\Delta p_{dis} = K_{dis}\frac{\rho_{dis}u_{dis}^2}{2} \tag{16}$$

In this case, this pressure tap is located very close to the outlet of the test section, in the region of recirculating flow, as shown in Fig. 2. Thus, reliable values for K_{dis} cannot be taken from the literature and a reverse approach is selected instead. For each experimental run i, Δp_{fric} is calculated based on the correlation from Cheng and Todreas (1986) and, subtracting all other terms from Eq. (8), individual estimated values for Δp_{dis} are obtained. Then, a mean value for K_{dis} of 0.3 is derived from Eq. (17).

$$K_{dis} = \frac{1}{N}\sum_{i}^{N}\left[\frac{\Delta P_{dis}}{0.5\rho_{dis}u_{b,dis}^2}\right]_i \tag{17}$$

With these considerations, the experimental results for the friction coefficient f are shown in Fig. 9 together with the correlation of Cheng and Todreas (1986).

Good agreement between the experimental data and the predicted values is found within ±10%. Furthermore, the solid line in Fig. 9 intersects the uncertainty interval of most data points. This is then a confirmation of LBE showing similar pressure drop characteristics as other fluid in bare rod-bundle geometries.

It should be noted that in both Figs. 8 and 9, relatively large uncertainties are observed for $\mathrm{Re} < 2\times10^4$. In that range, for such low values of $\dot{V}$ and Δp, the instrumentation is less accurate than for higher Re. Moreover, the range of the Reynolds numbers differs between Figs. 8 and 9 because the dynamic viscosity is evaluated at different temperatures, corresponding to the mean value throughout the flow section under consideration. In particular, the mean bulk temperature across the spacer was selected for Fig. 8 and the mean value across the complete bundle for Fig. 9. This results in a small difference in Re for heated tests.

4. Heat transfer analysis

Previous investigations on this subject are reviewed in Section 4.1. The evaluation method and experimental results of this work are presented in Sections 4.2 and 4.3, respectively.

4.1. Review of previous investigations

In the framework of fast-reactor development programs, several previous authors have published experimental results on liquid-metal heat transfer around bare rod bundles in a triangular array. Their data, partially reviewed in Weinberg (1975), Bobkov et al. (1988), and Mikityuk (2009), cover a wide range of operating parameters. For the sake of completeness, these are listed here in Table 3 and compared to the conditions of the present work. Additional experimental information is available for rod bundle with wire spacer, although this geometry is not directly comparable to the conditions of this campaign. A recent review on wire-wrap investigation is given by Roelofs et al. (2013).

It should be noticed that all the previous data listed in Table 3 have been presented at least 40 years ago, with no additional publications ever since. Unfortunately, some relevant information is not available (n.a.) in these publications. This database has been considered sufficiently extensive and the empirical correlations derived from it (see Appendix B) are satisfactorily accurate for sodium-cooled applications (Sesonske, 1972; Kirillov and Ushakov, 2001a). For current fast reactors and accelerator-driven-systems

Table 3
Previous experiments for liquid-metal heat transfer in triangular bare rod bundles (only $p/d \geq 1.1$). Data compiled from the listed sources. *Notes*: [*1] = 22/78. [*2] = 44/56. n.a. = information not available.

Year	Author(s)	Fluid	Rods (total)	p/d	Pr, –		$\mathrm{Re} \times 10^{-3}$, –		Pe, –		q_w, kW m^{-2}		T, °C	
					Min	Max	Min	Max	Min	Max	Min	Max	Min	Max
1961	Friedland et al.	Hg	19	1.38	0.016	0.021	8.0	80	190	1700	45	45	49	127
1961	Friedland et al.	Hg	13(19)	1.75	0.0227	0.0227	25	175	800	4000	~120		~38	
1963	Borishanskii and Firsova	Na	7	1.20	0.0057	0.0072	3.8	57	30	345	58	116	210	310
1964	Borishanskii and Firsova	Na	7	1.50	~0.0064		4.3	28	28	172	58	116	220	270
1964	Maresca and Dwyer	Hg	13	1.75	~0.02		7.5	200	150	4000	80	120	~38	
1965	Nimmo and Dwyer	Hg	13	1.75	n.a.	n.a.	n.a.	n.a.	150	4000	80	120	~38	
1967	Kalish and Dwyer	NaK[*1]	19	1.75	0.013	0.021	12	92	250	1200	58	96	135	343
1967	Zhukov et al.	Hg	7	1.10	~0.024		6.2	62	150	1500	n.a.	n.a.	n.a.	n.a.
1967	Zhukov et al.	Hg	7	1.20	~0.024		12.5	62	300	1500	n.a.	n.a.	n.a.	n.a.
1967	Zhukov et al.	Hg	7	1.30	~0.024		12.5	125	300	3000	n.a.	n.a.	n.a.	n.a.
1967	Zhukov et al.	Hg	7	1.40	~0.024		12.5	83	300	2000	n.a.	n.a.	n.a.	n.a.
1967	Zhukov et al.	Hg	7	1.50	~0.024		12.5	125	300	3000	n.a.	n.a.	n.a.	n.a.
1969	Hlavac et al.	Hg	13	1.75	0.019	0.022	29	175	550	3800	48	97	~38	
1969	Borishanskii et al.	Na	7	1.10	~0.007		18.4	76	130	530	82	166	219	224
1969	Borishanskii et al.	Na	7	1.30	~0.007		9.3	61	65	425	78	87	205	236
1969	Borishanskii et al.	Na	7	1.40	~0.007		13.6	47.2	95	330	81	166	200	225
1969	Borishanskii et al.	n.a.	7	1.10	~0.03		10.6	65	320	1950	81	139	207	220
1969	Borishanskii et al.	n.a.	7	1.30	~0.03		11.6	73.5	350	2200	75	93	206	222
1969	Borishanskii et al.	n.a.	7	1.40	~0.03		15.3	59.2	460	1780	93	151	208	230
1971	Subbotin et al.	Na	37	1.1	0.007	0.007	n.a.	n.a.	n.a.	n.a.	n.a.	n.a.	n.a.	n.a.
1972	Gräber and Rieger	NaK[*2]	31(37)	1.25	0.014	0.024	5.69	128	106	2700	~100		100	220
1972	Gräber and Rieger	NaK[*2]	31(37)	1.60	0.009	0.020	9.95	284	141	4300	~100		137	382
1972	Gräber and Rieger	NaK[*2]	31(37)	1.95	0.008	0.023	15.3	258	140	4300	~100		105	425
2013	This work	**LBE**	19	1.40	0.0184	0.0344	10.2	128	291	3060	118	**1033**	202	443

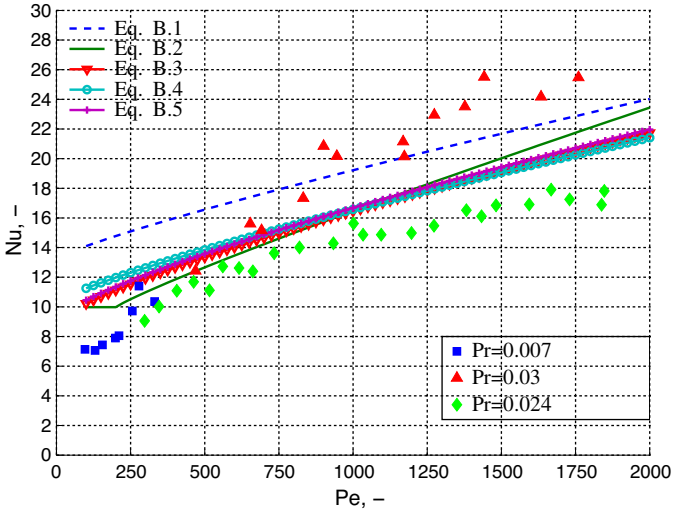

Fig. 10. Comparison of empirical correlations and experimental data (Borishanskii et al., 1969; Zhukov et al., 1967) for $p/d = 1.4$.

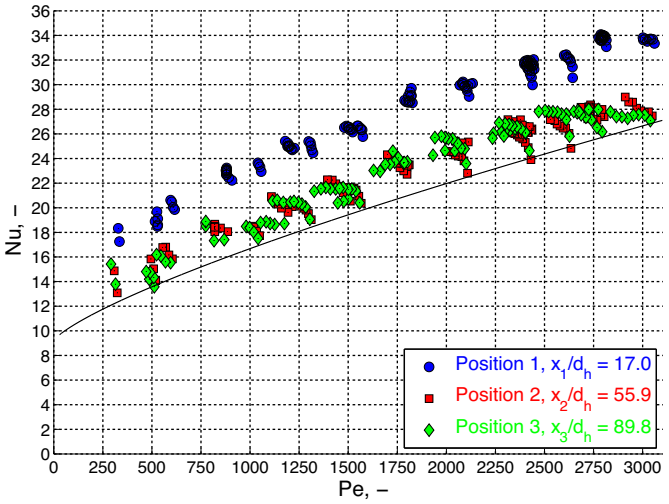

Fig. 11. Experimental Nu and Pe at three axial positions. The solid line represents the empirical correlation given by Eq. (B.5).

using either pure lead or LBE as coolants, this might not be the case. In that context, this work presents new, valuable data at reactor-like conditions in terms of temperature, velocity and heat flux density.

Some of these previous data, as well as the empirical correlations Eqs. (B.1)–(B.5) in Appendix B serve as a reference for evaluating our results in Section 4.3. As the pitch-to-diameter ratio has a large influence on the heat transfer (Reed, 1987), only the data with $p/d = 1.4$ from Zhukov et al. (1967) and Borishanskii et al. (1969) and correlations applied for this geometry are considered here, as shown in Fig. 10. It can be observed that the correlations given by Eqs. (B.3)–(B.5) are in good agreement with each other and with the experimental data. With this consideration, only Eq. (B.5) is considered for further reference in Section 4.3, because it is based on the most extensive database.

4.2. Evaluation method

In order to guarantee the comparability of these data with those of other authors, some details of the evaluation method are described in this section. Similarly to previous authors the hydraulic diameter of the inner subchannel, given by Eq. (18), is selected as the reference length for the heat transfer analysis.

$$d_h = d\left[\frac{2\sqrt{3}}{\pi}\left(\frac{p}{d}\right)^2 - 1\right] = 9.52\,\text{mm} \tag{18}$$

At each measuring plane, a local heat transfer coefficient α is defined as in Eq. (19), where $\langle T_w\rangle$ and T_b are the mean wall and bulk temperatures, respectively. On the one hand, $\langle T_w\rangle$ is the average of four thermocouples (see Section 2). On the other hand, T_b is derived from an energy balance throughout the test section (from the inlet until the position x), considering a temperature-dependent heat capacity as in Eq. (20).

$$\alpha = \frac{q_w}{\langle T_w\rangle - T_b} \tag{19}$$

$$Q\frac{x}{L} = \dot{m}\int_{T_{in}}^{T_b} c_p(T)dT \tag{20}$$

Based on the measurements, geometrical parameters and mean physical properties, non-dimensional local Nusselt and Péclet are formed as in Eqs. (21) and (22), respectively. In this case the physical properties (λ, c_p) are evaluated at the mean value between the inlet and the local bulk temperatures.

$$\text{Nu} = \frac{\alpha d_{h,sch}}{\lambda} \tag{21}$$

$$\text{Pe} = \frac{\dot{m}}{A}\frac{d_{h,sch}c_p}{\lambda} \tag{22}$$

with λ, c_p at $(T_{in} + T_b)/2$.

Moreover, a non-dimensional temperature Θ is defined as in Eq. (23). With this definition is $\Theta > 0$ at the wall and $\Theta < 0$ at the center of the subchannel.

$$\Theta = \frac{T - T_b}{q_w}\frac{\lambda}{d_h} \tag{23}$$

In this context, the mean wall non-dimensional temperature $\langle\Theta_w\rangle$ is the inverse of the Nusselt number. A hot-spot factor $\Phi \geq 1$ is defined as in Eq. (24) for indicating the relative magnitude of the maximum wall superheat.

$$\Phi = \frac{T_{w,\max} - T_b}{\langle T_w\rangle - T_b} = \frac{\Theta_{w,\max}}{\langle\Theta_w\rangle} = \Theta_{w,\max}\text{Nu} \tag{24}$$

4.3. Experimental results

Fig. 11 shows the experimental values of Nu and Pe at the three measuring planes, as defined in Section 4.2. Each of the three clouds of points follows a well-defined curve, without major deviations from the general trend. This is an indication of the good reproducibility of the measurements within the experimental uncertainties (for a detailed analysis, see Appendix C).

At a given Pe, Nu is remarkably larger (30–40%) at the first position than further downstream. Considering that this measuring point is relatively close to the beginning of the heated zone ($x_1/d_{h,sch} = 17$), this result can be explained by the flow being in the thermally developing region. Indeed previous authors, e.g. Maresca and Dwyer (1964), have observed that, following the flow development, Nu continuously decreases axially up to $x/d_{h,sch} = 25$.

The other two measuring positions are beyond this limit (even when considering the flow perturbations given by the spacers) and thus correspond to the fully developed region. This can be confirmed experimentally because similar values are observed in Fig. 11 for both positions. A good agreement between the experimental results and Eq. (B.5) is observed, with only a slight under-prediction (up to 20%). Remarkably, this equation agrees

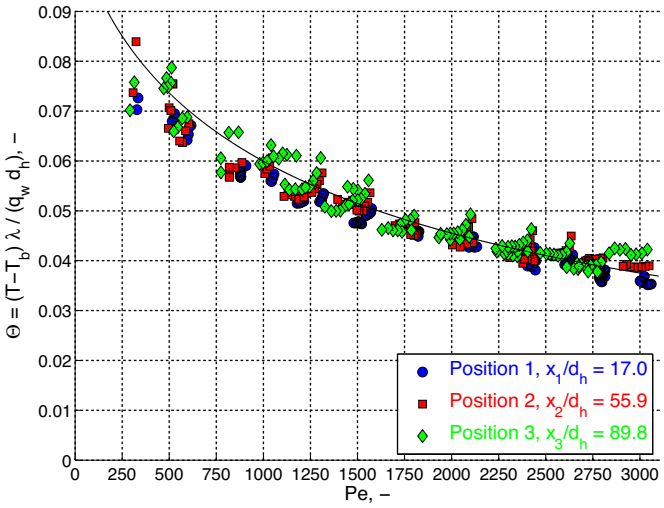

Fig. 12. Highest non-dimensional wall temperature ($\Theta_{w,\max}$) at each axial position as a function of Pe.

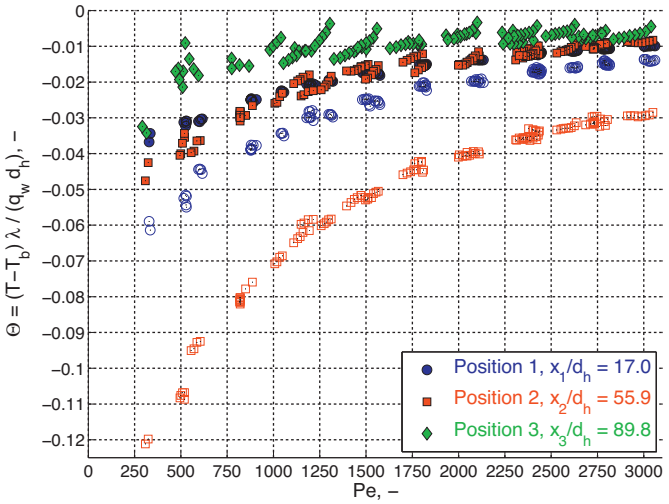

Fig. 13. Non-dimensional temperature Θ at the center of edge (empty symbols) and internal (colored) subchannels at each axial position as a function of Pe. (For interpretation of the references to color in this figure legend, the reader is referred to the web version of the article.)

better with the present results than with those from previous authors shown in Fig. 10, upon which it is partially based.

In addition to the heat transfer coefficient, hot spots are of main interest for the study of power-controlled systems. For this analysis, the highest wall temperature indicated by the eight thermocouples placed at each measuring plane (see Fig. 4) is shown in non-dimensional terms in Fig. 12. The mean wall superheat, i.e. Nu^{-1}, as predicted by the correlation Eq. (B.5) is indicated as a solid line for comparison.

It can be observed in Fig. 12 that in non-dimensional terms, the maximum wall superheat is similar at the three measuring levels. Furthermore, the solid line (designating $\langle\Theta_w\rangle = \mathrm{Nu}^{-1}$ as predicted by Eq. (B.5)) gives a good estimation of $\Theta_{w,\max}$. This agreement within ±10% between the experimental data points and the line is found throughout the entire range of Pe.

These results can also be analyzed in terms of the hot-spot factor Φ. A relatively wide range of $\Phi = 1.02$–1.40 is observed in this experimental work, without a clear dependence on Pe. In general, these hot spots are located at the central rod in the fully developed region (x_2 and x_3) and at the outer ring in the developing region (x_1). This experimental observation suggests caution when considering the Nu and Pe data from previous authors, as some measured the wall temperature only at the central rods (Maresca and Dwyer, 1964; Nimmo and Dwyer, 1965) and others at different positions (Gräber and Rieger, 1972).

A few considerations about the fluid temperature distribution can be derived from measurements at the positions indicated in Section 2.3. Fig. 13 shows these results in terms of Θ and Pe at the center of an edge (empty symbols) and the coldest internal (colored) subchannels.

For the internal subchannels, Θ gives an indication of how flat or rounded the temperature profile is. As a reference, $\Theta = 0$ corresponds to a uniform fluid temperature distribution at $T = T_b$, while a laminar profile in a circular duct yields $\Theta = -7/48 \approx -0.145$. For liquid metals, the low Pr leads to more rounded profiles, as the molecular heat conduction has a larger influence in the turbulent core than for higher Pr.

For the central subchannels, a minimum value of $\Theta_{\min} = -0.0475$ is observed at low Pe. At higher Pe, $\Theta_{\min}$ increases at the three axial positions, indicating that the temperature profile becomes more flat. This is a consequence of the larger turbulent conductivity, that becomes higher than the molecular one almost over the entire cross-section for higher Re (and thus Pe).

At both axial positions x_1 and x_2, the edge subchannel is remarkably colder than the internal ones. This is a logical consequence of the outer wall being unheated (this boundary condition is close to adiabatic, as the thermal losses are small), and turbulent mixing from the warmer internal channels being negligible for $p/d = 1.4$ (Rehme, 1992). The increase of Θ at higher Pe indicates a greater turbulent conductivity throughout the subchannel.

The results in Fig. 13 also indicate a large difference (roughly a factor two) between the values of Θ at the edge channels for x_1 and x_2. As this experimental information at this location is not available for x_3, see Fig. 4, some hypotheses can be formulated though not verified. At x_1, the flow is not yet fully developed and thus the velocity and temperature profiles are evolving. Furthermore, the study of the hot spots presented above in Fig. 12 indicated that at this axial position, the highest wall temperature is located at the outer ring. This result can be an indication of a non-homogeneous flow and temperature distribution at x_1, with a lower velocity at the edge channels. Such distribution can explain why the temperature at the center of this channel is, in terms of Θ higher at x_1 than at x_2.

5. Supplementary results

In this section, supplementary experimental information regarding the heat transfer at the third measuring level is evaluated. In particular, Section 5.1 presents results obtained moving the third spacer. The results obtained with the three thermocouples located inside the rod cladding are evaluated in Section 5.2.

5.1. Results moving the third spacer

The experimental setup allows to move the third spacer up to +90 and −120 mm around its reference position. However, as this spacer is placed near the end of the heated zone ($x_{sp,3,ref} = L_{heat} = 870$ mm), temperature measurements further downstream beyond this limit are not directly comparable with those obtained upstream.

Keeping all other operating parameters constant, these experiments allow to investigate the axial evolution of the flow. These results are shown in Fig. 14 for two different flow rates, corresponding to $\mathrm{Pe} = 778 \pm 9$ and $\mathrm{Pe} = 2680 \pm 30$.

As the flow develops thermally in the axial direction downstream of a perturbation (such as the grid spacers), the Nusselt

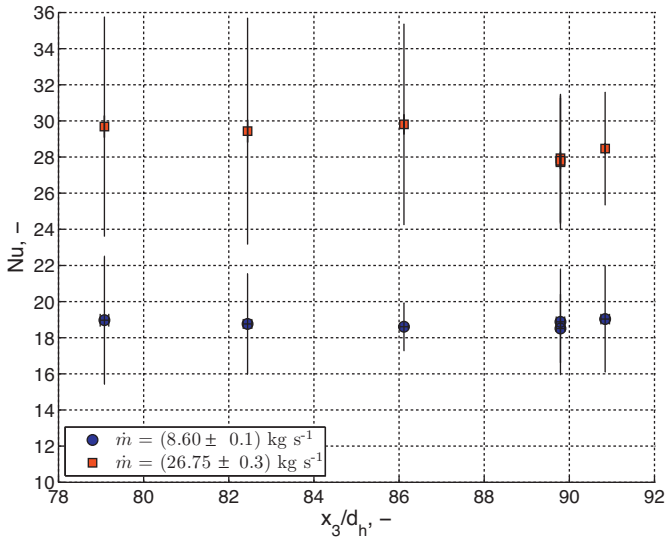

Fig. 14. Heat transfer results at different positions of the third spacer, for two different flow rates with T_{in} = 200 °C, and Q = 300 kW.

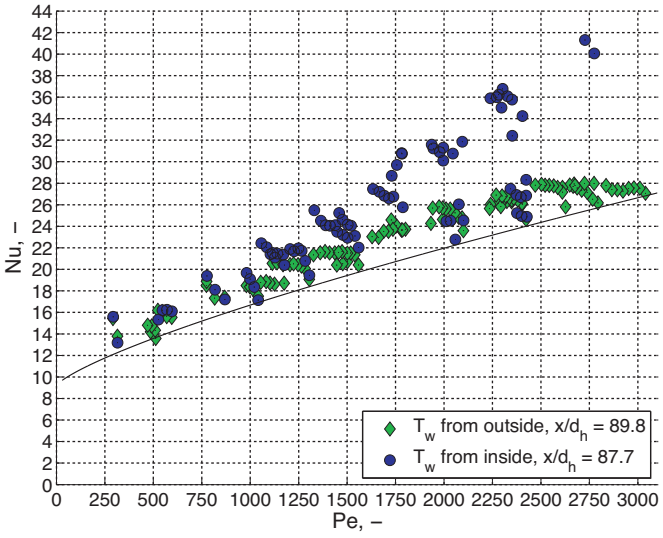

Fig. 15. Non-dimensional heat transfer results at the third spacer, obtained with two different measuring techniques for T_w. The solid line represents the empirical correlation given by Eq. (B.5).

number decreases asymptotically toward a constant value. The traditional criterion for establishing that the flow is thermally developed is when the differences in Nu are smaller than 5%, see e.g. Bhatti and Shah (1987).

Although some differences in Nu are observed in Fig. 14 (up to 6.8% for the largest flow rate), these are smaller than the experimental uncertainties (for details, see Appendix C). It can then be concluded that, under these conditions, these measurements represent the same physical variable, namely the Nusselt number for a fully developed flow.

A statistical average leads to Nu = 28.7 ± 0.9 (±3%) at the largest flow rate and Nu = 18.8 ± 0.2 (±1%) at the lowest flow rate. The low value of these deviations means that, within the uncertainties of the experiments, Nu remains constant at the considered axial positions.

This additional experimental information confirms that the flow is indeed fully developed at the third spacer. Considering that the second axial position x_2 has an even larger developing length downstream of the perturbation from the previous spacer, it can be safely assumed that the flow is also fully developed at the second spacer. Such conclusion can also be inferred from Fig. 11, where similar results are obtained at x_2 and x_3.

5.2. Results from the thermocouples located inside the wall

Among both techniques used for measuring T_w described in Section 2.3.1, those thermocouples *from outside* provided the most reliable information and their results were analyzed in Section 4. The ones placed inside the rod cladding, see Fig. 6, presented some experimental difficulties, discussed below.

On the one hand, these three thermocouples presented significant differences between each other. The deviations from their average is roughly twice as large as found with the thermocouples *from outside*, reaching values as large as $0.35(T_w - T_b)$, even if they are located at similar positions, see Fig. 4. These large deviations are reflected in the experimental uncertainty, as studied in Appendix C.

On the other hand, a relatively large correction given by Eq. (3) is required in order to avoid systematic errors. Furthermore, this correction relies on a strong assumption, i.e. that the temperature profile is dominated by radial thermal conduction through the thermocouple.

With these considerations, the results derived from these inner thermocouples are shown in Fig. 15 in terms of the Nusselt and Péclet numbers. For comparison, this figure also includes the results at x_3 *from outside*, displayed in Fig. 11 and considered reliable based on the analysis presented in the previous sections. It can be observed in this figure, that the results with T_w measured from inside the rod cladding can be divided into two groups as follows.

First, some results show good agreement between both methods. This is an indication that the conditions under which the correction given by Eq. (3) was developed are fulfilled. In other words, that the radial thermal conduction analysis presented in Section 2.3.1 is correct.

Second, some results present large differences between both methods, implying that Eq. (3) is not applicable. It should be noted that in these cases, Nu is overestimated, meaning that T_w is underestimated. In other words, Eq. (3) results in these cases in an over-correction. Furthermore, the differences are larger at higher Pe, implying that these measurements were influenced by the flow velocity, thus not fulfilling the conditions under which Eq. (3) was derived. Considering the steep temperature gradients throughout the rod cladding, both observations indicate that the positions of the thermocouples might not be perfectly fixed, even becoming in contact with the flowing LBE.

The existence of these two different groups is observed over a wide range of Pe, and for all the considered thermal powers and temperature levels. This means that, unfortunately, these measurements could not be well reproduced and no good criterion was found for determining a priori to which group one result belongs. In this work, this could only be determined a posteriori, comparing the two different implemented measuring techniques as in Fig. 15.

Based on this experience, it is recommended that, when embedding thermocouples inside the rod cladding, practical measures should be taken to fix its radial position within a very small tolerance. Following a purely radial thermal conduction analysis, Eq. (25) gives an estimation of the error introduced in Nu when the thermocouple position has an uncertainty Δy.

$$\frac{\mathrm{Nu}}{\mathrm{Nu}_{ref}} = \frac{1}{1 \pm (\Delta y / d_{h,sch}) \mathrm{Nu}_{ref}} \tag{25}$$

Considering reference values for $\mathrm{Nu}_{ref} < 30$ as shown in Fig. 11, a repeatability of Nu measurements within ±5% requires for this geometry, an uncertainty $\Delta y < 15$ μm. The results shown in Fig. 15

indicate that this condition was not fulfilled by the thermocouples located inside the wall.

Unfortunately previous authors who obtained their Nu measurements based on this technique alone for T_w, see Table 3, did not report this radial uncertainty nor the repeatability of their results. The present work indicate that the measurements *from outside* the cladding are more reliable than those *from inside*, see Figs. 11 and 15.

6. Concluding remarks

For the development and safety analysis of advanced nuclear systems based on heavy-liquid metals (lead or LBE), experimental information on flow and heat transfer in representative geometries under reactor-like conditions is essential in order to validate predicting tools. Nevertheless, reliable data are scarcely available in the literature and additional efforts are required in order to improve the understanding of the behavior of such flows.

This article describes an experimental campaign performed at the Karlsruhe Liquid Metal Laboratory (KIT-KALLA), consisting on an electrically heated 19-pin hexagonal rod bundle with three grid spacers, cooled by an upward LBE flow. A detailed description of the experimental setup is given in Section 2. Its two most remarkable and novel features can be summarized as follows. First, these experiments were performed at typical reactor conditions in terms of operating temperature (up to 450 °C), power density (up to 1.0 MW m^{-2}) and bulk velocity (2.2 m s^{-1}). Second, extensive detailed temperature measurements were installed at three axial levels, supported from above by the grid spacers. This construction allows measuring the rod wall temperature *from outside*, providing an accurate and reproducible representation of this sensitive variable.

The pressure drop measurements for both the spacers and distributed friction contributions are analyzed in Section 3. According to the work of Epiney et al. (2010) for sharp edge spacers, a correlation is derived for the spacer friction factor K_{sp} as a best fit of the present experimental data. In particular, the modified drag coefficient C_v was tuned to this particular spacer design. The experimental friction factors for the bare rod bundle show good agreement with the correlation of Cheng and Todreas (1986), with a deviation lower than ±10% and within the experimental uncertainties. In general, it is observed that, in non-dimensional terms, the results obtained in this work agree well with correlations developed for other fluids, mainly water, as expected. It should be noted that the data obtained at $\mathrm{Re} < 2\times10^4$ present a relatively larger uncertainty, see Figs. 8 and 9.

For the heat transfer analysis presented in Section 4, the results from this work can only be compared with others from liquid metals flow, due to their characteristically low Prandtl number. A review of previous investigations for similar configurations indicates that the available database is outdated and incomplete for LBE applications, as all these experiments were performed more than 40 years ago in alkali-metals and mercury systems. In the present work, considering the detailed experimental information derived from the thermocouples at the three spacers, a three-part analysis is presented.

Firstly, the mean heat transfer coefficient at each level is compared with empirical correlations in terms of Nu and Pe. At the second and third axial levels, similar results are obtained (indicating that the flow is fully developed), with Nu roughly 10% higher than predicted by Eq. (B.5). At the first axial position ($x_1/d_h = 17.0$), Nu is 30% higher for all Pe, indicating the flow is in the developing region. Secondly, hot spots factors up to $\Phi = 1.4$ are found at all the three levels. Furthermore, it is observed that the highest non-dimensional wall temperature $\Theta_{w,\max}$ is within ±10% of the mean value (i.e. Nu^{-1}) predicted by Eq. (B.5). Thirdly, the non-dimensional temperature at the center of internal and edge sub-channels are found to increase at higher Pe. These results indicate an increase in the turbulent thermal diffusivity and shall serve for the validation of numerical tools.

Supplementary experimental information was analyzed in Section 5, with the following observations. Firstly, by moving the third spacer slightly around its reference position, it can be confirmed that the flow is indeed fully developed, as the Nusselt number remains constant. Secondly, comparing the heat transfer results with both measuring techniques for T_w, it is observed that the thermocouples placed *outside* the wall are more reliable than those located *inside* the rod cladding, and some recommendations for improving this reliability are given.

In summary, an extensive and successful experimental campaign at reactor-like operating conditions was completed, following the need for reliable data for LBE flow and heat transfer in fuel-assembly representative geometries. The results from this work present a high level of confidence, derived from their good repeatability within the experimental uncertainties.

Acknowledgment

The authors would like to acknowledge the support of the European Union in the framework of the EU 7th framework project THINS, grant number 249337.

Appendix A. Physical properties

In all cases, the temperature-dependent physical properties of LBE were evaluated using the empirical correlations recommended in the LBE-Handbook (Nuclear Energy Agency, 2007). For the sake of completeness, these formulas are detailed in Table 4. In all cases, SI units are considered.

Appendix B. Heat transfer correlations

The most relevant correlations for LM heat transfer in triangular rod bundles have been reviewed in Pfrang and Struwe (2007) and Mikityuk (2009). For the sake of completeness, they are listed in the following paragraphs, where $\mathcal{X} = p/d$.

A semi-empirical model was developed by Dwyer (1969), covering the wide range of $70 < \mathrm{Pe} < 10,000$ and $1.3 < \mathcal{X} < 3.0$ as in Eq. (B.1).

$$\mathrm{Nu} = 6.66 + 3.126\mathcal{X} + 1.184\mathcal{X}^2 + 0.0155(\psi\mathrm{Pe})^{0.86} \tag{B.1}$$

Table 4
Physical properties of LBE as a function of temperature (T in Kelvin), from LBE-Handbook (Nuclear Energy Agency, 2007).

Property	Symbol	Expression	Uncertainty	Value at 300 °C
Density	$\rho(T)$	$11096 - 1.3236T$	≤0.8%	10,337 kg m^{-3}
Heat capacity	$c_p(T)$	$159 - 2.72\,10^{-2}T + 7.12\,10^{-6}T^2$	≤7.0%	145.7 J kg^{-1} K^{-1}
Thermal conductivity	$\lambda(T)$	$3.61 + 1.517\,10^{-2}T - 1.741\,10^{-6}T^2$	≤5.0%	11.7 W m^{-1} K^{-1}
Dynamic viscosity	$\mu(T)$	$4.94\,10^{-4}\exp(754.1/T)$	≤5.0%	0.0018 kg m^{-1} s^{-1}
Prandtl number	$\mathrm{Pr}(T)$	$c_p(T)\mu(T)\lambda^{-1}(T)$	?	0.023

with

$$= 1 - \frac{1.82}{\mathrm{Pr}(\epsilon_M/\nu)_{\max}^{1.4}}$$

and

$$\ln\left(\frac{\epsilon_M}{\nu}\right)_{\max} = 0.864 \ln \mathrm{Re} - 0.24\mathcal{X} - 2.12$$

Based on their own experimental data, Borishanskii et al. (1969) postulated Eq. (B.2), valid for Pe < 2000 and $1.1 \leq \mathcal{X} \leq 1.5$.

$$\mathrm{Nu} = \begin{cases} \mathrm{Nu}_1 & \text{if Pe} < 200 \\ \mathrm{Nu}_1 + \mathrm{Nu}_2 & \text{if Pe} > 200 \end{cases} \tag{B.2}$$

$$\mathrm{Nu}_1 = 24.15 \log(-8.12 + 12.75\mathcal{X} - 3.65\mathcal{X}^2)$$

$$\mathrm{Nu}_2 = 0.0174[1 - e^{-6(\mathcal{X}-1)}](\mathrm{Pe} - 200)^{0.9}$$

Eq. (B.3) was proposed by Gräber and Rieger (1972), as a best fit of their own data, covering the range 150 < Pe < 4000 and $1.2 < \mathcal{X} < 2.0$.

$$\mathrm{Nu} = 0.25 + 6.2\mathcal{X} + (-0.007 + 0.032\mathcal{X})\mathrm{Pe}^{0.8-0024\mathcal{X}} \tag{B.3}$$

For $\mathcal{X} > 1.3$, the correlation by Ushakov et al. (1977) is reduced to Eq. (B.4), applicable for Pe < 4000 and $\mathcal{X} < 2.0$.

$$\mathrm{Nu} = 7.55\mathcal{X} - 20\mathcal{X}^{-13} + \frac{3.67}{90\mathcal{X}^2}\mathrm{Pe}^{0.56+0.19\mathcal{X}} \tag{B.4}$$

Recently, Mikityuk (2009) compiled experimental data from several authors and proposed Eq. (B.5) as a fit for the wide range $1.1 < \mathcal{X} < 1.95$ and 30 < Pe < 5000.

$$\mathrm{Nu} = 0.047(1 - e^{-3.8(\mathcal{X}-1)})(\mathrm{Pe}^{0.77} + 250) \tag{B.5}$$

Appendix C. Uncertainty analysis

For primary and secondary variables derived from them, the uncertainty is propagated as follows. Let Y be a secondary variable which depends on a set of N primary variables X_i as in Eq. (C.1). Assuming that these contributions are independent from each other, the standard deviation of Y is given by Eq. (C.2). For a detailed description of the uncertainty analysis, the reader is referred to Moffat (1988).

$$Y = f(X_1, \ldots, X_N) \tag{C.1}$$

$$\sigma_Y^2 = \sum_{i=1}^{N}\left(\frac{\partial f}{\partial X_i}\right)^2 \sigma_{X_i}^2 \tag{C.2}$$

With these considerations, the mean and maximum standard deviation for the studied variables are summarized in Table 5.

It can be observed that the uncertainties of the secondary variables are larger than that of the primary variables. This is a direct consequence of the uncertainty propagation expressed by (C.2). It should also be noted that these non-dimensional variables, are calculated relying on the physical properties (listed in Table 4). Their uncertainties have a dominant effect for Re and Pe, which show the same relative values at the three axial positions.

The temperature measurements, obtained at a fast sampling rate of 2000 Hz, showed statistical uncertainties in the range 0.3–2.0 K. The magnitude of this uncertainty is reflected in the relative uncertainty of Nu listed in Table 5. Nevertheless, it should be noted that the mean values indicated in Fig. 11 repeated at different heat fluxes present much lower differences. In that context, these points overlap within the uncertainty intervals, which were not included in Fig. 11 for the sake of clarity. As discussed in Section 5.2, an issue affecting the temperature measurements is the thermocouple position. Furthermore, it is assumed that the thermocouples represent the temperature at its center, where the sensing tip is located.

Table 5
Uncertainties of the studied variables.

Variable	$\langle\sigma_X\rangle$	$\max(\sigma_X)$	$\langle\frac{\sigma_X}{X}\rangle$	$\max\left(\frac{\sigma_X}{X}\right)$
Primary variables				
Q	2.3 kW	13.9 kW	1.5%	12.5%
$\Delta P_{sp,1}$	1.32 mbar	1.68 mbar	1.75%	10.97%
$\Delta P_{sp,2}$	1.30 mbar	1.65 mbar	1.77%	11.21%
$\Delta P_{sp,3}$	1.33 mbar	2.61 mbar	1.84%	10.78%
ΔP_{tot}	7.2 mbar	11.87 mbar	1.51%	16.1%
$\dot{V}$	0.06 $m^3\,h^{-1}$	0.14 $m^3\,h^{-1}$	1.25%	12.6%
Secondary variables – pressure drop				
Re_1	2.9 10^3	4.9 10^3	5.2%	8.4%
Re_2	3.1 10^3	5.4 10^3	5.2%	8.4%
Re_3	3.3 10^3	5.8 10^3	5.2%	8.4%
$K_{sp,1}$	0.046	0.31	3.0%	17.4%
$K_{sp,2}$	0.046	0.30	3.0%	17.6%
$K_{sp,3}$	0.049	0.31	3.1%	17.3%
f	0.0021	0.0284	9.3%	100%
Secondary variables – heat transfer				
Pe_1	100.6	159.9	5.4%	13.6%
Pe_2	98.4	159.3	5.4%	13.6%
Pe_3	95.8	158.8	5.4%	13.6%
Nu_1	4.3	11.5	14.1%	33.4%
Nu_2	2.7	7.6	11.3%	27.1%
Nu_3	4.1	10.5	16.9%	37.2%

References

Bhatti, M.S., Shah, R.K., 1987. Turbulent and transition flow convective heat transfer in ducts. In: Kakaç, S., Shah, R.K., Aung, W. (Eds.), Handbook of Single-Phase Convective Heat Transfer. John Wiley & Sons Inc. (Chapter 4).

Bobkov, V., Vinogradov, V., Kozina, N., 1988. Analysis of data and recommendations on heat transfer by liquid metals in rod bundles. Sov. Atom. Energy 65 (6), 1007–1011.

Borishanskii, V., Firsova, E.V., 1963. Heat exchange in the longitudinal flow of metallic sodium past a tube bank. Sov. Atom. Energy 14 (6), 614–615.

Borishanskii, V., Firsova, E.V., 1964. Heat exchange in separated bundles of rods with metallic sodium flowing longitudinally. Sov. Atom. Energy 16 (5), 562–563.

Borishanskii, V., Gotovskii, M., Firsova, E.V., 1969. Heat transfer to liquid metals in longitudinally wetted bundles of rods. Sov. Atom. Energy 27 (6), 1347–1350.

Cheng, S.-K., Todreas, N.E., 1986. Hydrodynamic models and correlations for bare and wire-wrapped hexagonal rod bundles – bundle friction factors, subchannel friction factors and mixing parameters. Nucl. Eng. Des. 92 (2), 227–251.

Chenu, A., Mikityuk, K., Chawla, R., 2011. Pressure drop modeling and comparisons with experiments for single- and two-phase sodium flow. Nucl. Eng. Des. 241 (9), 3898–3909.

Cigarini, M., Dalle Donne, M., 1988. Thermohydraulic optimization of homogeneous and heterogeneous advanced pressurized water reactors. Nucl. Technol. 80 (1), 107–132.

Dwyer, O., 1969. Heat transfer to liquid metals flowing in-line through unbaffled rod bundles: a review. Nucl. Eng. Des. 10 (1), 3–20.

Eifler, W., Nijsing, R., 1980. Experimental and Analytical Studies on the Single Phase Flow Characteristics of the 12-Rod Sodium Boiling Test Section. Euratom -publications- EU. Harwood Academic Publishers.

Epiney, A., Mikityuk, K., Chawla, R., 2010. TRACE qualification via analysis of the EIR gas-loop experiments with smooth rods. Ann. Nucl. Energy 37 (6), 875–887.

Friedland, A., Dwyer, O.E., Maresca, M.W., Bonilla, C.F., 1961. Heat transfer to mercury in parallel flow through bundles of circular rods. In: In: International Heat Transfer Conference. Number Paper No. 62, Boulder (CO, USA).

Gräber, H., Rieger, M., 1972. Experimentelle Untersuchung des Wärmeübergangs an Flüssigmetalle (NaK) in parallel durchströmten Rohrbündeln bei konstanter und exponentieller Wärmeflußdichteverteilung. Atomkernenergie 19 (1), 23–40 [in German]. English title: Experimental investigation of the heat transfer on liquid metals (NaK) in parallel flow through rod bundles under constant and exponential heat flux distribution.

Hlavac, P., Dwyer, O., Helfant, M., 1969. Heat transfer to mercury flowing in line through an unbaffled rod bundle: experimental study of the effects of rod displacement on rod-average heat transfer coefficients. J. Heat Transfer 91, 568–580.

Johnson, H., Hartnett, J., Clabaugh, W., 1953. Heat transfer to molten lead-bismuth eutectic in turbulent pipe flow. Trans. Am. Soc. Mech. Eng. 75 (6), 1191–1198.

Kalish, S., Dwyer, O.E., 1967. Heat transfer to NaK flowing through unbaffled rod bundles. Int. J. Heat Mass Transfer 10 (11), 1533–1558.

Kirillov, P., Ushakov, P., 2001a. Heat transfer to liquid metals: specific features, methods of investigation, and main relationships. Therm. Eng. 48 (1), 50–59.
Kirillov, P.V., Ushakov, P.A., 2001b. Liquid-metal heat transfer in rod bundles. Therm. Eng. 48 (2), 127–133.
Lefhalm, C., Knebel, J., Mack, K., 2001. Kinetics of gas phase oxygen control system (OCS) for stagnant and flowing Pb–Bi systems. J. Nucl. Mater. 296 (1), 301–304.
Maresca, M.W., Dwyer, O.E., 1964. Heat transfer to mercury flowing in-line through a bundle of circular rods. J. Heat Transfer 86 (2), 180–186.
Mikityuk, K., 2009. Heat transfer to liquid metal: review of data and correlations for tube bundles. Nucl. Eng. Des. 239 (4), 680–687.
Moffat, R.J., 1988. Describing the uncertainties in experimental results. Exp. Therm. Fluid Sci. 1 (1), 3–17.
Möller, R., Tschöke, H., 1972. Theoretische Untersuchungen zur Wandtemperaturmessung an simulierten Brennstäben für thermodynamische Experimente in Natrium. Technical Report KFK1555, Kernforschungszentrum Karlsruhe [in German]. English title: Theoretical investigation of wall temperature measurements on fuel rod simulators for thermohydraulic experiments in sodium.
Nimmo, B., Dwyer, O., 1965. Heat transfer to mercury flowing inline through a rod bundle. J. Heat Transfer 87, 312–313.
Nuclear Energy Agency, 2007. Handbook on Lead-bismuth Eutectic Alloy and Lead Properties, Materials Compatibility, Thermal-hydraulics and Technologies. OECD/NEA Nuclear Science Committee Working Party on Scientific Issues of the Fuel Cycle Working Group on Lead-bismuth Eutectic.
Pfrang, W., Struwe, D., 2007. Assessment of correlations for heat transfer to the coolant for heavy liquid metal cooled core designs. Technical Report FZKA 7352, Forschunszentrum Karlsruhe GmbH.
Reed, C., 1987. Convective heat transfer in liquid metals. In: Kakaç, S., Shah, R.K., Aung, W. (Eds.), Handbook of Single-Phase Convective Heat Transfer. John Wiley & Sons, Inc (Chapter 8).
Rehme, K., 1972. Pressure drop performance of rod bundles in hexagonal arrangements. Int. J. Heat Mass Transfer 15 (12), 2499–2517.
Rehme, K., 1992. The structure of turbulence in rod bundles and the implications on natural mixing between the subchannels. Int. J. Heat Mass Transfer 35 (2), 567–581.
Rehme, K., Trippe, G., 1980. Pressure drop and velocity distribution in rod bundles with spacer grids. Nucl. Eng. Des. 62, 349–359.
Roelofs, F., Gopala, V.R., Jayaraju, S., Shams, A., Komen, E., 2013. Review of fuel assembly and pool thermal hydraulics for fast reactors. Nucl. Eng. Des. 265, 1205–1222.
Sesonske, A., 1972. Heat transfer in liquid-metal cooled fast reactors. Adv. Nucl. Sci. Technol. 6, 175–201.
Subbotin, V.I., Zhukov, A.V., Pashek, M., Sviridenko, E.Y., Ushakov, P.A., Shults, V., 1971. Experimental study on models of the operating temperature regimes of the fuel elements of a BOR-60 reactor. Heat Transfer – Sov. Res. 3 (5), 15–26.
Ushakov, P., Zhukov, A., Matyukhin, N., 1977. Heat transfer to liquid metals in regular arrays of fuel elements. High Temp. (USSR) 15 (10), 1027–1033.
Voj, P., Markfort, D., Ruppert, E., Dwyer, O.e., 1973. Thermal-Hydraulic Analysis for Fuel Elements with Liquid-Metal Cooling.
Weinberg, D., 1975. Temperaturfelder in Bündeln mit Na-Kühlung. In: In: Thermo- und fluiddynymische Unterkanalanalyse der Schnellbrüter-Brennelemente und ihre Relation zur Brennstabmechanik, pp. 167–202 [in German]. English title: Temperature fields in sodium-cooled bundles.
Zhukov, A.V., Subbotin, V.I., Ushakov, P.A., 1967. Heat transfer from loosely-spacer [fuel] rod clusters to liquid metal flowing in the axial direction. In: Kirillov, P.L., Subbotin, V.I., Ushakov, P.A. (Eds.), Liquid Metals. National Aeronautic and Space Administration (translated from Atomizdat), pp. 149–169.